Millimeter-Wave Sparse Imaging for Concealed Objects Based on Sparse Range Migration Algorithm

Li Ding, Shuxian Wu, Ping Li, and Yiming Zhu

***Abstract*— To relieve the system cost in densely sampling when applying the millimeter-wave (MMW) synthetic aperture radar (SAR) technique for imaging applications, an MMW sparse imaging method is presented by the combination of the under-sampling scheme in space and the following sparse imaging algorithm. Different from the requirement on sub-wavelength sampling interval by Nyquist law, the system only needs to collect a random subset of spatial samples. To transform the spatial samples into wavenumber domain, a sparse range migration algorithm (SRMA) is proposed to realize MMW sparse imaging by embedding the matrix completion (MC) technique into classical RMA. In light of the relationship of Fourier transform between the scattering coefficients and the wavenumber-domain echo, the proposed algorithm utilizes the atomic norm minimization to fulfill the MC from the small set of wavenumber-domain entries to their full data matrix. The experiments are conducted by a wideband MMW transceiver mounted on a linear trajectory for imaging two specimens with different kinds of cover. Their clear imaging contrast of azimuth-range profiles is obtained through SRMA under different under-sampling conditions and RMA with fully sampled data, and verify the effectiveness of the proposed method.**

***Index Terms*— MMW sparse imaging, sparse range migration algorithm, atomic norm minimization, matrix completion, under sampling.**

I. Introduction

Recently, because of the advantage to penetrate through non-metallic materials, such as clothing, concrete or packaging materials and the comparable resolution capability, millimeter-wave (MMW) imaging has received increasing interest [1]. In the field of MMW imaging by synthetic aperture radar (SAR) technique, range migration algorithm (RMA) is a kind of Fourier transform (FT)-based algorithm, which is popular to provide a high-resolution imaging. However, its requirement by Nyquist law with densely sampling in spatial domain aggravates the system costs as well as the signal acquisition time. This situation, hence, is intensified in the MMW band especially because of the small sampling interval when further increasing the signal frequency for higher resolution. This motivates the development of effective imaging approach that requires only a sparse subset of spatial samples instead of their full sets.

Currently there are plenty of studies focusing on the sparse inversion problem with respect to the limited samples [2]–[13], and one of the most popular methods is matrix completion (MC) technique. Compared with the other sparse techniques, such as compressed sensing (CS) [4]–[6], [14], MC provides a different way in dealing with the under-determined problem from the perspective of lost-data restoration, which estimates the missing data by inspecting the relationship between the observed elements and the unobserved ones [7]–[9]. It is independent of the measurement-matrix design which is a key factor determining the performance of CS [6]. Research shows that MC has been demonstrated high accuracy to recover the missing data from partial entries by taking advantage of low rank constraint [15]–[24]. So far, MC technique has been widely applied in various fields, such as far-field SAR imaging [17], collaborative filtering [18], system identification [20], spectrum sensing [21], sparse channel estimation [22], sensor network [23], multimedia coding and communication [24], and so on. Nevertheless, to the best of our knowledge, there is relatively less work to introduce MC technology into MMW applications.

Motivated by the above considerations, in the paper, we propose a MMW sparse imaging method by combing the MC technique to allow the spatial under-sampling when utilizing one-dimensional (1-D) SAR in azimuth. Specially, the imaging system mainly consists of a MMW transceiver which emits the wideband MMW signals and is mounted on a linear trajectory to fulfill the near field scanning. In this way, the transmitted wideband signal contributes to the range resolution, and the motion of the transceiver contributes to the azimuth resolution by synthetic aperture technique. The MMW transceiver is

Manuscript received February 21, 2019; accepted April 17, 2019. Date of publication April 22, 2019; date of current version July 17, 2019. This work was supported in part by the National Natural Science Foundation of China under Grant 61731020, Grant 61605113, and Grant 61601291, in part by the National Program on Key Basic Research Project of China (973 Program) under Grant 2014CB339806, in part by the Major National Development Project of Scientific Instrument and Equipment under Grant 2016YFC1202505, in part by the Natural Science Foundation of Shanghai under Grant 16ZR1423100, in part by the Shanghai Leading Talent under Grant 2016019, and in part by the Young Yangtse Rive Scholar. The associate editor coordinating the review of this paper and approving it for publication was Dr. Laura Anitori. *(Corresponding author: Yiming Zhu.)*

L. Ding, P. Li, and Y. Zhu are with the Terahertz Technology Innovation Research Institute, Shanghai 200093, China, also with the Shanghai Key Lab of Modern Optical System, University of Shanghai for Science and Technology, Shanghai 200093, China, and also with the Terahertz Science Cooperative Innovation Center, Shanghai 200093, China (e-mail: ymzhu@usst.edu.cn).

S. Wu is with the Terahertz Technology Innovation Research Institute, Shanghai, China.

Digital Object Identifier 10.1109/JSEN.2019.2912642

placed not far from the object under the test, while the motion trail is parallel to the front surface of the target. Considering this short distance between the transceiver and the object, there is a near-field imaging problem. Based on the stationary phase theorem, the double round-trip distance in raw echo can be decomposed to result in a 2-D analytical expression for MMW near-field imaging in the wavenumber domain. To achieve the sparse imaging based on the partial measurements by spatially under-sampling, a sparse RMA (SRMA) is proposed by embedding MC into the classical RMA. In light of Fourier transformation relationship between the scattering coefficients and the wavenumber-domain echo, the embedded MC step is achieved by an atomic-norm minimization method to exactly recover the fully 2-D wavenumber-domain data set [25]. Hence, different from the rigorous requirement on sub-wavelength sampling interval by classical RMA, this improved algorithm allows the sparse sampling, either to speed up the measurement or to reduce the amounts of measurements.

This proposed imaging method is then applied for concealed-object detection. Two kinds of steel specimens with different covers are laboratory-made. One specimen is a steel covered by the concrete, and the other is two steels covered by a packing box. Both the simulations and experiments are conducted the signal in the 30 GHz - 35 GHz bandwidth. The results demonstrate that this proposed algorithm can provide a good azimuth-range imaging profile, and verify its effectiveness for MMW sparse imaging.

The remainder of this paper is organized as follows. In the next section, the MMW imaging system is presented. In section III, the SRMA based on atomic norm minimization is introduced in detail. In section IV, we provided the numerical simulation and clear experimental results to verify the effectiveness of the proposed algorithm. Finally, the conclusion is drawn in section V.

II. MMW Sparse Imaging System

The diagram of the considered MMW near-field imaging system is shown in Fig. 1. The transceiver is mounted on a linear trail, which locates in a short range from the specimen. The motion trajectory of the transceiver is linear and parallel to the X-axis. In this paper, we focus on the azimuth and range dimensions of the targets, and thus only XOY plane is concerned.

Let $(x', -R_0)$ be a spatial sampling point of the transceiver, and $x' \in [L_x/2, L_x/2]$, where L_x denotes the observation aperture length in azimuth dimension and R_0 indicates the distance between the observation plane and the target.

The transceiver emits stepped-frequency (SF) signals, and its p-th transmitted signal is

$$s_p(t) = \mathrm{e}^{j2\pi f_p t} \tag{1}$$

where f_p is the operating frequency, and $f_p = f_0 + (p-1)\Delta f$, f_0 and Δf denote the starting frequency and the frequency step, respectively, $p = 1, 2, \cdots, P$.

Letting a general scatterer on the targets be at position (x, y) and with the complex reflection coefficient $\sigma(x, y)$, the echo

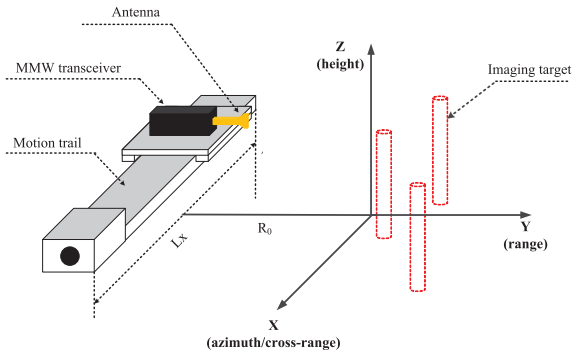

Fig. 1. The diagram of MMW imaging system.

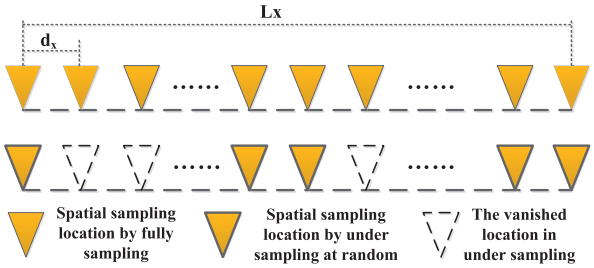

Fig. 2. Random down-sampling locations.

received at the position $(x', -R_0)$ and then it would be turned to a zero IF signal by down conversion, i.e., $I + jQ$. The corresponding receiving signal to the p-th frequency is shown as

$$\begin{aligned} s_p(x') &= \iint_{x,y} \sigma(x, y)\, \mathrm{e}^{j2\pi f_p\left(t - \frac{2R(x')}{c}\right)} \cdot \mathrm{e}^{-j2\pi f_p t} dxdy \\ &= \iint_{x,y} \sigma(x, y)\, \mathrm{e}^{-j2\pi f_p \frac{2R(x')}{c}} dxdy \end{aligned} \tag{2}$$

where $R(x')$ denotes the distance between the scatterer and the transceiver, i.e., $R(x') = \sqrt{(x - x')^2 + (y + R_0)^2}$, and c is the wave velocity.

For MMW sparse imaging, as Fig.2 shows, we take the under-sampling samples as the partial entries of the fully observed samples required by Nyquist theory. That is, at each frequency point, the data obtained by spatially sampling the signal (2) on densely uniform grids is denoted as $\mathbf{s}_{p,\mathbf{\Omega}} = [s_{p,1}, \cdots, s_{p,N}]^T$, where $\mathbf{\Omega}$ denotes the location set of those uniform grids in space, i.e., $\mathbf{\Omega} = \{1, 2, \cdots, N\}$, and N denotes the number of full data set at each frequency. Such that $s_{p,n}$ is observed if and only if $n \in \mathbf{\Omega}$, and each entry $s_{p,n}$ is expressed as

$$\begin{aligned} &s_{p,n} \\ &= \iint_{x,y} \sigma(x, y)\, \mathrm{e}^{-j2k_p\sqrt{(x-(n-1)\cdot d_x+L_x/2)^2+(y+R_0)^2}} dxdy \end{aligned} \tag{3}$$

where k_p denotes the wave number, $k_p = 2\pi\frac{f_p}{c}$, d_x denotes the sub-wavelength sampling interval of the observation aperture in X-dimension, and $L_x = (N-1)d_x$.

Algorithm 1 Classical RMA [26].

Input:

Receive zero-IF echo over the frequency and spatial domains, $s_p(x')$, $p = 1, \cdots, P$, $x' \in [-L_x/2, L_x/2]$;

Output:

1: Take the spatial 1-D Fourier-transform of $s_p(x')$ along x' to form the angular spectrum at each frequency,

$$z\left(k_x, k_p\right) = \int_{x'} s_p(x') \mathrm{e}^{-jk_x x'} dx' \tag{5}$$

where k_p denotes the wave number, $k_p = 2\pi \frac{f_p}{c}$, and k_x is the wave-number component in the X-dimension.

2: Apply the phase compensation to the angular spectrums based on the method of stationary phase,

$$z\left(k_x, k_p\right) = z\left(k_x, k_p\right) \mathrm{e}^{-jk_y R_0} \tag{6}$$

where k_y denotes the wave-number component in the Y-dimension, and $k_y = \sqrt{4k_p^2 - k_x^2}$.

3: Turn the non-uniform $z\left(k_x, k_y\right)$ to uniform $\dot{z}\left(k_x, k_y\right)$ by Slot interpolation.

4: Take the 2-D inverse FT of $\dot{z}\left(k_x, k_y\right)$ to achieve the imaging

$$\hat{\sigma}\left(x, y\right) = \iint_{k_x, k_y} \dot{z}\left(k_x, k_y\right) \mathrm{e}^{jk_x x} \mathrm{e}^{jk_y y} dk_x dk_y \tag{7}$$

5: **return** $\hat{\sigma}\left(x, y\right)$.

When allowing spatially down sampling, it is assumed that $\boldsymbol{\Omega}$ is sampled at random. For convenience, we define the location subset of $\boldsymbol{\Omega}$ as $\boldsymbol{\mathcal{L}}$. That is, $\boldsymbol{\mathcal{L}} \subseteq \boldsymbol{\Omega}$. Then, it yields a data subset as

$$\mathbf{s}_{p,\boldsymbol{\mathcal{L}}} = P_{\boldsymbol{\mathcal{L}}} \odot \mathbf{s}_{p,\boldsymbol{\Omega}} \tag{4}$$

where $\odot$ denotes the Hadamard product, $P_{\boldsymbol{\mathcal{L}}}$ is the projection operator of the size the same as $\mathbf{s}_{p,\boldsymbol{\Omega}}$, denoting the orthogonal projection of $\mathbf{s}_{p,\boldsymbol{\Omega}}$ onto the subspace of vectors determined by $\boldsymbol{\mathcal{L}}$. Specifically, the n-th entry of $P_{\boldsymbol{\mathcal{L}}}$ equals 1 if $n \in \boldsymbol{\mathcal{L}}$, or equals 0, otherwise. It is found that $\mathcal{P}_{\boldsymbol{\mathcal{L}}}$ vanishes the entries outside $\boldsymbol{\mathcal{L}}$.

III. Sparse Range Migration Algorithm

By collecting the echoes over all the spatial sampling positions and all the frequency samples, the classical RMA according to (2) is shown in detail in Algorithm 1 [26]. Because RMA assumes fully observed uniformly-spaced spatial samples for imaging, the short wavelength of MMW leads to the significant cost increase of data acquisition. Therefore, inspired by the low-rank MC, we propose to adopt the under-sampling in space to allow reducing the amount of measurement data far below its Nyquist required quantities.

Therefore, by collecting the spatially undersampled echoes from all the transmitted SF signals, the SRMA is given in detail in Algorithm 2. It is obvious from (11) to observe that the under-sampling in spatial X-dimension can be equivalently converted to that in the corresponding wavenumber domain. Also, the semi-definite programming (SDP) can be used to solve this atomic-norm minimization, which has a much

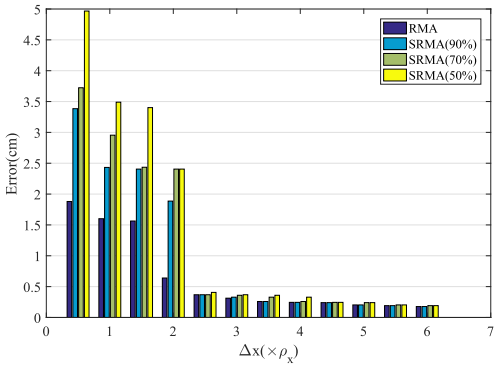

Fig. 3. Imaging performance in light of azimuth resolution, K = 2, $\rho_x = 1.78cm$.

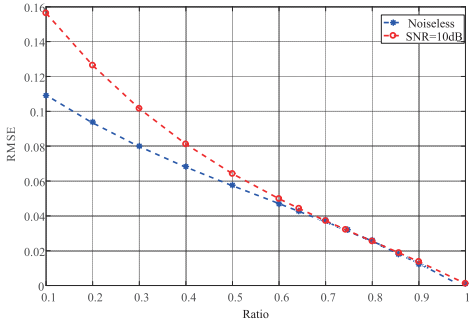

Fig. 4. Atomic-norm minimization performance for reconstructing wavenumber samples for the letter W case, K = 9.

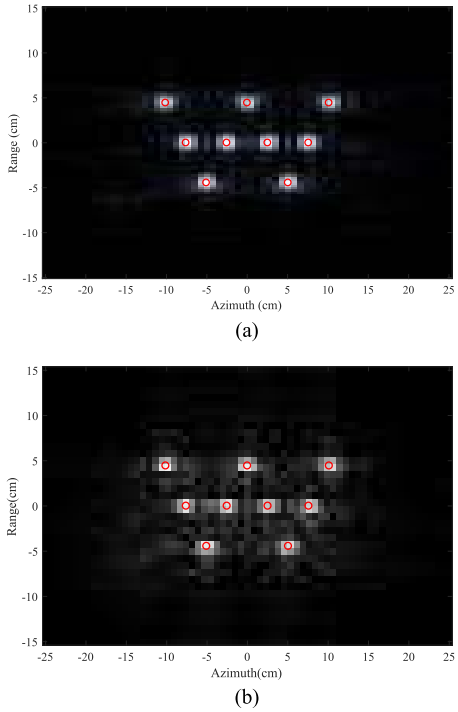

Fig. 5. Numerical simulation results of the letter W. (a) RMA, full data. (b) SRMA, random sampling with 70% of full data.

clearer form as

$$\min_{\mathbf{z},\mathbf{T},u} \frac{1}{2}tr(\mathbf{T}) + \frac{1}{2}u$$
$$s.t. \begin{bmatrix} \mathbf{T} & \mathbf{z} \\ \mathbf{z}^* & u \end{bmatrix} \geq 0, \quad P_{\mathcal{L}} \odot \mathbf{z} = \bar{\mathbf{z}}_{p,\mathcal{L}} \tag{8}$$

where $\mathbf{T}$ is a Hermitian matrix, and $u > 0$ (see [6] for more information).

Algorithm 2 Sparse RMA.

Input:

Receive zero-IF echo over the frequency and spatial domains, $\mathbf{s}_{p,\mathcal{L}}$, $p = 1, \cdots, P$;

Output:

1: Take the 1-D non-uniformly discrete Fourier-transform of $\mathbf{s}_{p,\mathcal{L}}$ to form the discrete angular spectrum at each frequency,

$$\bar{z}(p,l) = \sum_{n\in\mathcal{L}} s_{p,n} \mathrm{e}^{-jk_x(l)\left((n-1)\cdot d_x - \frac{L_x}{2}\right)} \tag{9}$$

where $\bar{z}(p,l)$ denotes the wavenumber sample corresponding to the p-th frequency and the n-th spatial sampling location, $k_x(l) = l \cdot \Delta k_x$, $l \in \mathcal{L}$, $\Delta k_x = 2k_{x,max}/N$, and $k_{x,max}$ denotes the wavenumber span in X dimension;

2: Apply the phase compensation to the under-sampled angular spectrums,

$$\bar{z}(p,l) = \bar{z}(p,l)\mathrm{e}^{-jk_y(p,l)R_0} \tag{10}$$

where $k_y(p,l) = \sqrt{4k_p^2 - k_x^2(l)}$.

3: At each frequency point, take the atomic norm on $\bar{\mathbf{z}}_{p,\mathcal{L}}$ to achieve matrix completion,

$$\min \ \|\mathbf{z}\|_{\mathcal{A}}$$
$$s.t. \ P_{\mathcal{L}} \odot \mathbf{z} = \bar{\mathbf{z}}_{p,\mathcal{L}} \tag{11}$$

where $\|\cdot\|_{\mathcal{A}}$ denotes the atomic norm, $\bar{\mathbf{z}}_{p,\mathcal{L}} \in \mathcal{C}^{N\times 1}$ denotes the vector of the stacked wavenumber samples at the p-th frequency point, and its l-th entry takes the value of (10) if $l \in \mathcal{L}$ and otherwise, takes the value of 0. The solution of (11) is denoted as $\hat{\mathbf{z}}_p$, and $\hat{\mathbf{z}}_p = [\hat{z}(p,1), \cdots, \hat{z}(p,N)]^T$ which indicates the reconstructed full-sampling wavenumber samples.

4: Similarly to Algorithm 1.3, insert the non-uniform $\hat{z}(p,n)$ to a uniform form $\hat{z}(p',n')$ by Slot interpolation, where $\hat{z}(p',n')$ is wavenumber samples located on uniform grid of (k_x, k_y).

5: Similarly to (7), take the 2-D inverse FT of $\hat{z}(p',n')$ to achieve the imaging.

6: **return** $\hat{\sigma}(x,y)$.

In (10), $k_{x,max}$ is the maximal expansion of wavenumber domain in X-dimension and usually can be computed as $k_{x,max} = 2k_0 \sin(\frac{\theta_{eff}}{2})$, $k_0 = 2\pi\frac{f_0}{c}$, where the f_0 is the central frequency of the bandwidth signal, $\theta_{eff} = \min\{\theta_{3dB}, \theta_{span}\}$, θ_{3dB} and θ_{span} denote the 3 dB beamwidth of the adopted antenna and the spanned aperture angle by aperture length, respectively. Then, assume that there are K scatterers in the scene. According to the Theorem I.1 in [6] and (10), we would similarly have that

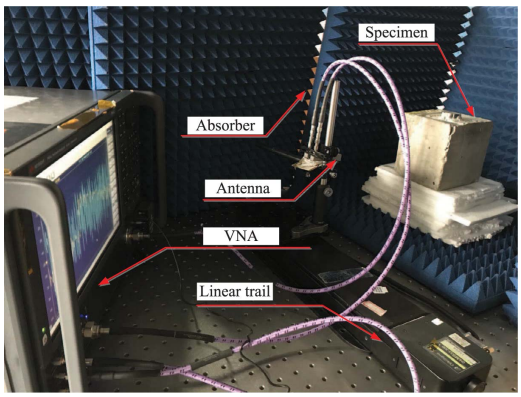

(a)

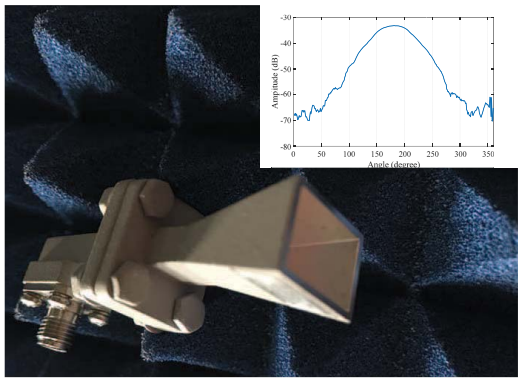

(b)

Fig. 6. MMW-based experimental system. (a) Photograph of the MMW-based experimental system. (b) Photograph of horn antenna and its radiation pattern.

Proposition 1: If the azimuth distance between any two scatterers is greater than $\frac{2\pi}{2k_{x,max}/4}$, *then for*

$$|\mathcal{L}| \geqslant C \max\left(\log^2\frac{N}{\delta}, K\log\frac{K}{\delta}\log\frac{N}{\delta}\right)$$

with a numerical constant C, the reconstruction in (11) suffices for a good recovery performance with probability at least 1-δ, where $|\cdot|$ *computes the entry number of a set.*

The proof is seen in Appendix I.

IV. Simulations and Experiments

The first simulation is conducted to validate our imaging method and to evaluate the performances of the proposed algorithms. The simulation frequency ranges from 30 GHz to 35 GHz with 5 GHz bandwidth, the number of frequency points is $P = 80$. The range distance R_0 is set as 25 cm. The synthesized aperture length is $L_x = 30$ cm, and the interval of sampling elements is $d_x = 4.5$ mm. Such that the number of full spatial samples at each frequency point is $N = 71$. Therefore, by letting the azimuth resolution and the range resolution be denoted as ρ_x and ρ_y, respectively, they can be computed as

$$\rho_x = \frac{\pi}{k_{x,max}} = 1.78 \text{ cm}, \quad \rho_y = c/2B = 3 \text{ cm}$$

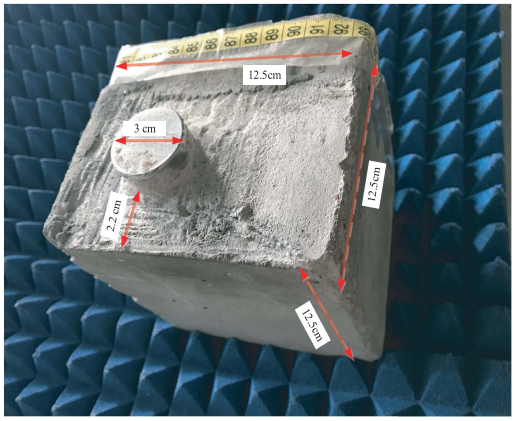

Fig. 7. Photograph of the specimen of one steel.

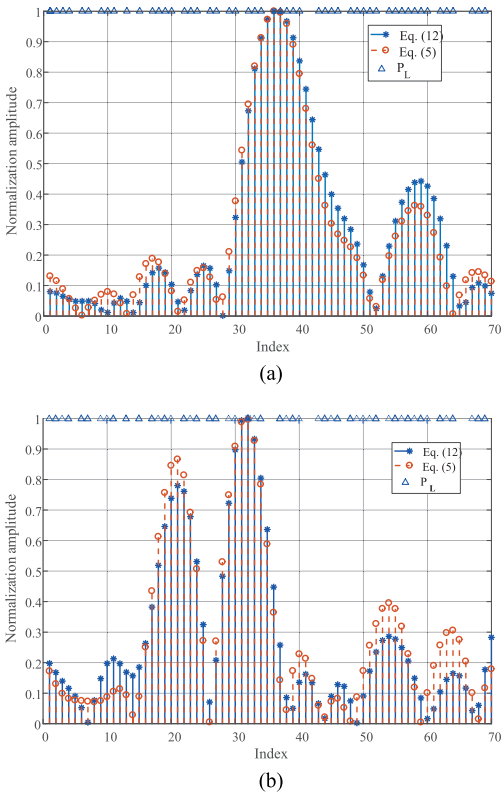

Fig. 8. Comparison between the reconstructed $\hat{\mathbf{z}}_p$ by atomic-norm minimization i.e., (11) and its corresponding full data $\mathbf{z}_p$, i.e., (6) at frequency 32.5 GHz. (a) Real part. (b) Imaginary part.

where $k_{x,max} = 2k_0 \sin\left(\frac{\theta_{eff}}{2}\right)$, k_0 denotes the wavenumber at the center frequency 32.5 GHz, $\theta_{3dB} = 30^o$ and $\theta_{span} = 2\tan^{-1}\left(\frac{L_x/2}{R_0}\right) = 62^o$ [26], [27].

The proposition 1 implies a quantitative amount denoting the reduced samples which can be estimated through a numerical way for the discrete objects case. However, considering the difficulty to get the prior of the number of scatterers in practice, here we numerically show the relationship of the imaging performance with respect to the actual number by examining the X-dimensional resolution. In Fig.3, there are two scatterers (i.e., K = 2) with the same range and the varying X-dimensional distance, which is denoted as Δ_x. The estimation error is computed in an absolute way

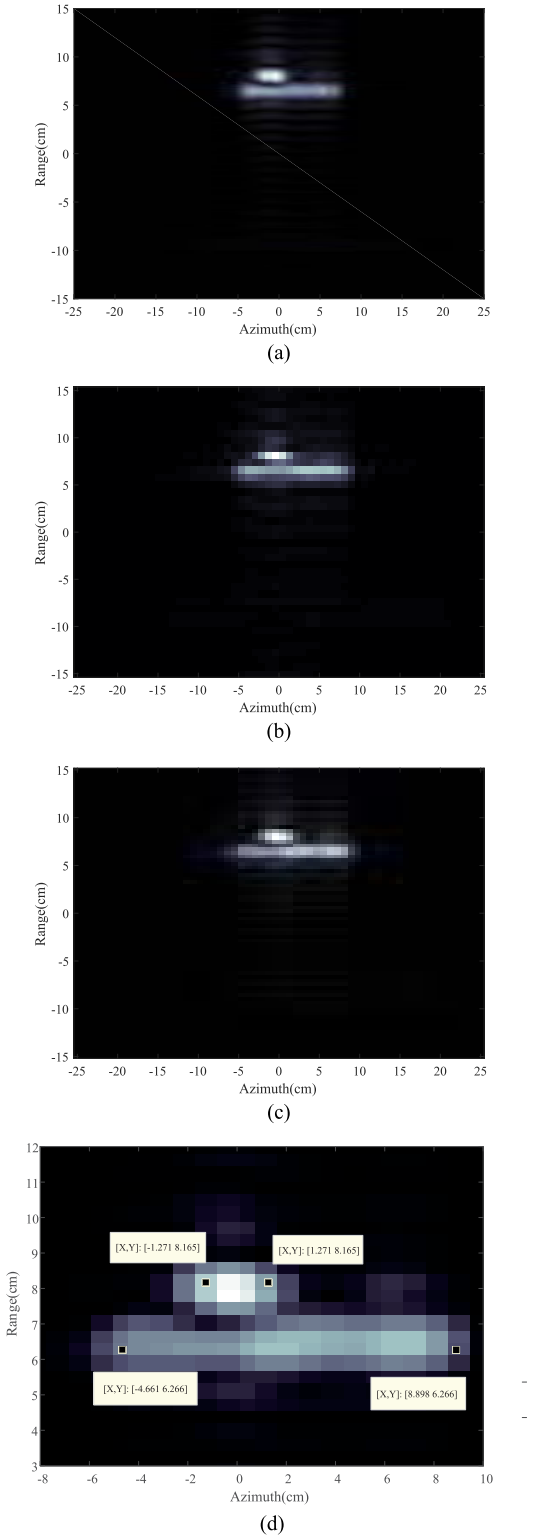

Fig. 9. Imaging results for the specimen of reinforced concrete wall. (a) RMA, full data. (b) SRMA, random sampling with 70% of full data. (c) SRMA, random sampling with 60% of full data. (d) Zoom in of (c).

as $\sum_{k=1}^{2} \left|x_k - \hat{x}_k\right|$. The comparison among the SRMA with different size of subset indicates that in the current case when the subset contains about 70% of full data, the imaging performance can be stable. Besides, the Proposition 1 implies

Fig. 10. Photograph of the specimen of two steels.

that the resolution in X dimension would be degraded by the extra constant of 4. Even though, we can numerically have that the azimuth resolution can be better. Fig. 3 numerically illustrates that the imaging performance by SRMA can be consistent with RMA when the distance Δ_x increases over 2.5 times of ρ_x.

Furthermore, for the multiple scatterers simulation of a letter W, as Fig. 4 shows, there is $K = 9$. With the aforementioned parameters, the reconstruction performance by equation (11) is examined in terms of root-mean-square error (RMSE), i.e.,

$$\sqrt{\frac{1}{P}\sum_{p=1}^{P}\left\|\mathbf{z}_p - \hat{\mathbf{z}}_p\right\|_2^2}$$

where $\mathbf{z}_p$ denotes the stacked wavenumber samples at the p-th frequency in the case of full data, and the ratio is computed as the entry number of the sub-position set $\boldsymbol{\mathcal{L}}$ over that of the full-position set $\boldsymbol{\Omega}$. Fig. 4 shows that when the subset increases to about 70% of the full data under the condition of SNR $= 10$ dB, the matrix completion in wavenumber domain can get the reconstruction performance similar to the noiseless case. Then, the imaging performance comparison between SRMA and RMA is illustrated. It is found from Fig. 5 (b) that given a subset of samples, SRMA is able to achieve the imaging performance comparable with that obtained by RMA with full samples.

The proof-of-principle experiment of MMW imaging system is developed in the 30 GHz-35 GHz band, as Fig. 6 (a) shows. A MMW vector network analyzer (VNA) is taken as the broadband heterodyne transceiver to couple the MMW signal into the transmitting horn and to exact the return wave from the receiving antenna for imaging. Two horn antennas are mounted next to each other on a linear trail to simulate a monostatic scanning. The radiation pattern and the photograph of antenna are shown in Fig.6 (b), where the 3 dB beamwidth at frequency 32.5 GHz is about 30^o and the y-axis label shows the measured amplitude of S21 parameter. All the involved parameters are the same as that in simulation. The output power of VNA is limited and is about 8 mW. The echo SNR of VNA is about 10 dB. Specimen's position is not far from

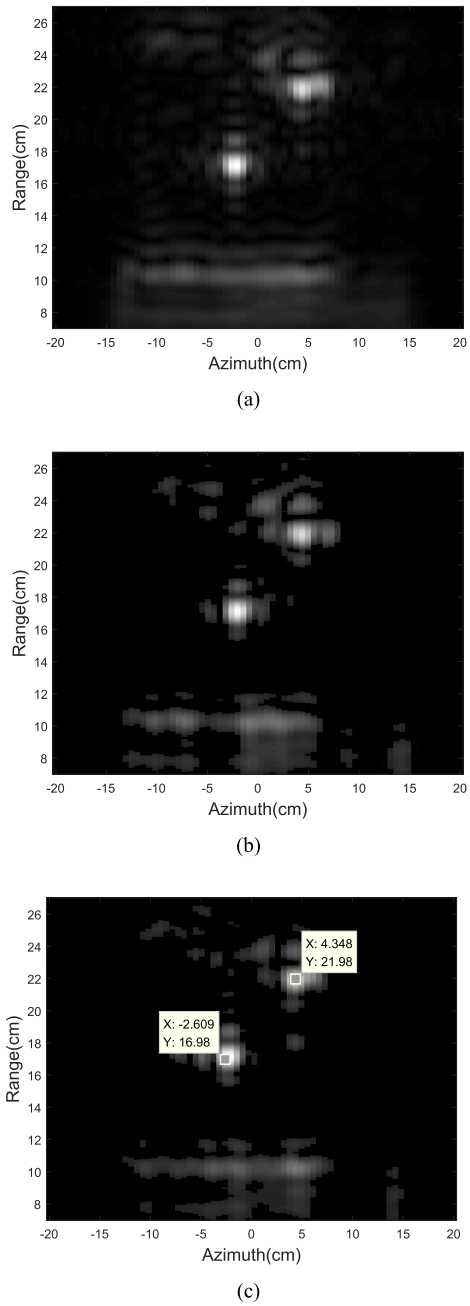

Fig. 11. Imaging results for two steels covered by a packing box. (a) RMA, full data. (b) SRMA, random sampling with 70% of full data. (c) SRMA, random sampling with 60% of full data.

the antenna's aperture, i.e., $R_0 = 20$ cm, and the trail length is $L = 30$ cm.

The first target is a laboratory-produced steel specimen, shown in Fig.7. The cover of the steel is mainly composed of cement and sand with ratio of one to two, and the specimen dimension is 12.5 cm$\times$12.5 cm$\times$12.5 cm. The cylindrical steel reinforcement has a diameter of 3 cm, in which the distance from its center position to the test front surface of the specimen is 2.2 cm. The reconstruction of wavenumber-domain samples, i.e., (11), is firstly examined. Fig. 8 compares the reconstructed wavenumber samples of $\hat{\mathbf{z}}_p$ by equation (11) in SRMA and the wavenumber samples of $z(k_x, k_p)$ by

equation (6) in RMA. The actual number of spatial samples used in (11) is 70% of the full data set. Obviously, it shows that atomic-norm-minimization based MC technology can achieve a high-performance reconstruction of data. The imaging results are shown in Fig. 9 (a), (b)and (c), which verify that MMW near-field imaging system can provide the capability of the steel reinforcement imaging. In Fig. 9 (d), four positions cursors are given, from which the size of the specimen and the depth between the steel and the concrete cover can be roughly estimated as 13.5 cm and 2.54 cm, respectively. Although not exactly matched with the true locations, due to the possible factors such as the expansion of the point spread function, the depth smaller than the range resolution, the multiple path effective between the steel and concrete cover and so on, these two estimated values are reliable.

To further verify the feasibility of our algorithm for the MMW imaging of multiple targets, two steels placed inside a paper box are used as the other specimen for the experiment, shown in Fig.10. The distance between the two steels is about 7 cm in azimuth and 5 cm in range direction. Similar to the experiment above, the imaging results are shown in Fig. 11(a), (b) and (c). Obviously, the front surface of the packaging box with a length of 20 cm is estimated at the position of 10 cm in range dimension, while the steel which is closer to the antenna is estimated as 17 cm in range dimension, since then the relative distance is exactly 7 cm, just as the real setup. Furthermore, as Fig. 11(c) shows, two position cursors indicate the location of two steels and also illustrate that the relative position between them are consistent with the reality.

In short, compared with the results by classical RMA through full sampling by Nyquist law, the proposed SRMA can maintain a comparable imaging performance with reduced measurements. Both the two experimental results show that the proposed method can brings a huge reduction in practical sampling for the MMW imaging application.

V. Conclusion

This paper has proposed a SRMA method by coupling the atomic-norm-minimization-based matrix completion technique and RMA for MMW sparse imaging. It allows the under-sampling in space to break out the limitation of Nyquist law for the reflectivity profile reconstruction. The experiments have been conducted on concealed objects detection, and two laboratory-made specimens with steel are taken as the imaging objects. Then, the results have confirmed the feasibility and effectiveness of the proposed MMW sparse imaging method. Although the use of atomic-norm-minimization makes the sample reduction by only one third or so, the proposed algorithm improves the classical RMA in dealing with the under-determined imaging problem and expands its applications into MMW sparse imaging. Especially in the case of the MMW band, due to the great difference between the short wavelength and common size of objects, this method can still play an important role to reduce the signal acquisition cost and to simplify the operation complexity in some situations. Furthermore, this method can be expanded into 3-D imaging cases by adopting the 2-D scanning mechanism and the 2-D matrix completion technology in the detection of concealed target, which will be studied in future work.

Appendix I
Proof of Proposition 1

Theorem 2 [6]: Suppose we observe the signal

$$x_n^* = \sum_{k=1}^{K} c_k e^{j2\pi f_k n}, \quad n = 0, \ldots, N-1$$

with unknown frequencies $\{f_1, \cdots, f_K\} \subset [0, 1]$ *on an index set* $T \subset \{0, \cdots, n-1\}$ *of size* m *selected uniformly at random. Additionally, assume* $sign(c_k) := c_k/|c_k|$ *are drawn i.i.d. from the uniform distribution on the complex unit circle and*

$$\Delta f = \min_{k_1 \neq k_2} \left| f_{k_1} - f_{k_2} \right|$$

where the distance $|f_{k_1} - f_{k_2}|$ *is understood as the wrap-around distance on the unit circle. If* $\Delta f \geqslant \frac{1}{[(N-1)/4]}$, *then there exists a numerical constant* C *such that*

$$m \geqslant C \max \left\{ \log^2 \frac{N}{\delta}, K \log \frac{K}{\delta} \log \frac{N}{\delta} \right\}$$

is sufficient to guarantee that we can recover x^* *and localize the frequencies via a semidefinite program with probability at least 1-*δ *with respect to the random samples and signs.*

With respect to the signal in (10), it can be simplified in a more enlightening way by stationary phase method such as

$$\bar{z}(p, l) = \sum_{k=1}^{K} \sigma_k e^{-jk_x(l)x_k - jk_y(p,l)y_k} \tag{12}$$

where $k_x(l)$ and $k_y(p, l)$ denote the l-th X-dimensional and the (p, l)-th Y-dimensional wavenumber component, respectively. Due to the data reconstruction occurs at each frequency, that is, at the p-th frequency, (12) can be expressed as a function of variable l

$$\bar{z}_p(l) = \sum_{k=1}^{K} \tilde{\sigma}_{p,k} \mathrm{e}^{-jk_x(l)x_k} \tag{13}$$

where $\tilde{\sigma}_{p,k} \approx \sigma_k \mathrm{e}^{-jk_y(p,l)y_k}$, $k_x(l) = \frac{2k_{x,\max}}{N} l$, $l \in \boldsymbol{\mathcal{L}}$, and $k_{x,max}$ denotes the wavenumber span in X dimension.

The exponential term in (13) can be rewritten as $k_x(l)\, x_k = 2\pi \frac{2k_{x,\max}}{2\pi N} x_k l$. If the atomic-norm-minimization (11) can reconstruct the full-sampling wavenumber data $\hat{\mathbf{z}}_p$ from $|\boldsymbol{\mathcal{L}}|$ samples, i.e., $\bar{z}_p(l)$ selected at random on the index $\boldsymbol{\Omega}$, according to the Theorem 2, it requires that

$$\min_{k_1 \neq k_2} \frac{2k_{x,\max}}{2\pi N} \left| x_{k_1} - x_{k_2} \right| \geqslant \frac{1}{(N-1)/4} \tag{14}$$

Then for rather great N, $N - 1 \approx N$ holds, and we can have a concise form of (14) as

$$\min_{k_1 \neq k_2} \left| x_{k_1} - x_{k_2} \right| \geqslant \frac{2\pi}{2k_{x,\max}/4}$$

Therefore, combining Theorem 2, the Proposition 1 can be proven.

REFERENCES

[1] M. Nezadal, J. Adametz, and L.-P. Schmidt, "Wideband imaging systems in the MM-wave and THz range for security and nondestructive testing," in *Proc. 31st URSI Gen. Assem. Sci. Symp.*, Aug. 2014, pp. 1–4.

[2] H. L. de Moura, D. R. Pipa, A. D. N. Wrasse, and M. J. D. Silva, "Image reconstruction for electrical capacitance tomography through redundant sensitivity matrix," *IEEE Sensors J.*, vol. 17, no. 24, pp. 8157–8165, Dec. 2017.

[3] Z. Shi, C. Zhou, Y. Gu, N. A. Goodman, and F. Qu, "Source estimation using coprime array: A sparse reconstruction perspective," *IEEE Sensors J.*, vol. 17, no. 3, pp. 755–765, Feb. 2017.

[4] H. Zamani and M. Fakharzadeh, "1.5-D sparse array for millimeter-wave imaging based on compressive sensing techniques," *IEEE Trans. Antennas Propag.*, vol. 66, no. 4, pp. 2008–2015, Apr. 2018.

[5] S. D. Babacan *et al.*, "Compressive passive millimeter-wave imaging," in *Proc. IEEE Int. Conf. Image Process.*, Sep. 2011, pp. 2705–2708.

[6] G. Tang, B. N. Bhaskar, P. Shah, and B. Recht, "Compressed sensing off the grid," *IEEE Trans. Inf. Theory*, vol. 59, no. 11, pp. 7465–7490, Nov. 2013.

[7] L. Zhang *et al.*, "Resolution enhancement for inversed synthetic aperture radar imaging under low SNR via improved compressive sensing," *IEEE Trans. Geosci. Remote Sens.*, vol. 48, no. 10, pp. 3824–3838, Oct. 2010.

[8] S.-J. Wei, X.-L. Zhang, J. Shi, and G. Xiang, "Sparse reconstruction for SAR imaging based on compressed sensing," *Prog. Electromagn. Res.*, vol. 109, pp. 63–81, Sep. 2010.

[9] E. J. Candes, J. Romberg, and T. Tao, "Robust uncertainty principles: Exact signal reconstruction from highly incomplete frequency information," *IEEE Trans. Inf. Theory*, vol. 52, no. 2, pp. 489–509, Feb. 2006.

[10] M. Moallem and K. Sarabandi, "Polarimetric study of MMW imaging radars for indoor navigation and mapping," *IEEE Trans. Antennas Propag.*, vol. 62, no. 1, pp. 500–504, Jan. 2014.

[11] L. Xiao, D. Jiang, D. Xu, H. Zhu, Y. Zhang, and H. V. Poor, "Two-dimensional antijamming mobile communication based on reinforcement learning," *IEEE Trans. Veh. Technol.*, vol. 67, no. 10, pp. 9499–9512, Oct. 2018.

[12] X. Wu, W.-P. Zhu, and J. Yan, "Direction of arrival estimation for off-grid signals based on sparse Bayesian learning," *IEEE Sensors J.*, vol. 16, no. 7, pp. 2004–2016, Apr. 2016.

[13] L. Xiao, Q. Yan, W. Lou, G. Chen, and Y. T. Hou, "Proximity-based security techniques for mobile users in wireless networks," *IEEE Trans. Inf. Forensics Security*, vol. 8, no. 12, pp. 2089–2100, Dec. 2013.

[14] B. Gonzalez-Valdes *et al.*, "Sparse array optimization using simulated annealing and compressed sensing for near-field millimeter wave imaging," *IEEE Trans. Antennas Propag.*, vol. 62, no. 4, pp. 1716–1722, Apr. 2014.

[15] E. J. Candes and B. Recht, "Exact low-rank matrix completion via convex optimization," in *Proc. 46th Annu. Allerton Conf. Commun., Control, Comput.*, Sep. 2009, pp. 806–812.

[16] E. J. Candes and Y. Plan, "Matrix completion with noise," *Proc. IEEE*, vol. 98, no. 6, pp. 925–936, Jun. 2010.

[17] D. Yang, G. Liao, S. Zhu, X. Yang, and X. Zhang, "SAR imaging with undersampled data via matrix completion," *IEEE Geosci. Remote Sens. Lett.*, vol. 11, no. 9, pp. 1539–1543, Sep. 2014.

[18] K. Barman and O. Dabeer, "Analysis of a collaborative filter based on popularity amongst neighbors," *IEEE Trans. Inf. Theory*, vol. 58, no. 12, pp. 7110–7134, Dec. 2012.

[19] E. Bojnordi and P. Moradi, "A novel collaborative filtering model based on combination of correlation method with matrix completion technique," in *Proc. 16th CSI Int. Symp. Artif. Intell. Signal Process.*, May 2012, pp. 191–194.

[20] N. E. Zubov, E. A. Mikrin, M. S. Misrikhanov, V. N. Ryabchenko, S. N. Timakov, and E. A. Cheremnykh, "Identification of the position of an equilibrium attitude of the international space station as a problem of stable matrix completion," *J. Comput. Syst. Sci. Int.*, vol. 51, no. 2, pp. 291–305, Apr. 2012.

[21] J. Meng, W. Yin, H. Li, E. Houssain, and Z. Han, "Collaborative spectrum sensing from sparse observations using matrix completion for cognitive radio networks," in *Proc. IEEE Int. Conf. Acoust., Speech Signal Process.*, Mar. 2010, pp. 3114–3117.

[22] M. O. Khalifa, A. H. Abdelhafiz, and A. Zerguine, "Sparse channel estimation using adaptive filtering and compressed sampling," in *Proc. Int. Conf. Comput., Elect. Electron. Eng.*, Aug. 2013, pp. 144–147.

[23] F. Fazel, M. Fazel, and M. Stojanovic, "Random access sensor networks: Field reconstruction from incomplete data," in *Proc. Inf. Theory Appl. Workshop*, Feb. 2012, pp. 300–305.

[24] S. Pudlewski and T. Melodia, "On the performance of compressive video streaming for wireless multimedia sensor networks," in *Proc. IEEE Int. Conf. Commun.*, May 2010, pp. 1–5.

[25] Y. Chi and Y. Chen, "Compressive two-dimensional harmonic retrieval via atomic norm minimization," *IEEE Trans. Signal Process.*, vol. 63, no. 4, pp. 1030–1042, Feb. 2015.

[26] J. M. Lopez-Sanchez and J. Fortuny-Guasch, "3-D radar imaging using range migration techniques," *IEEE Trans. Antennas Propag.*, vol. 48, no. 5, pp. 728–737, May 2000.

[27] D. M. Sheen, D. L. McMakin, and T. E. Hall, "Three-dimensional millimeter-wave imaging for concealed weapon detection," *IEEE Trans. Microw. Theory Techn.*, vol. 49, no. 9, pp. 1581–1592, Sep. 2001.

Li Ding received the bachelor's and master's degrees from the University of Electronic Science and Technology of China, Chengdu, China, in 2008, and the Ph.D. degree from the University of Science and Technology of China, Hefei, China, in 2011.

She is currently an Assistant Professor with the University of Shanghai for Science and Technology, Shanghai, China. Her research interests include millimeter-wave and terahertz-wave technology, especially with the applications to target detection and imaging.

Shuxian Wu is currently pursuing the master's degree in optical engineering with the University of Shanghai for Science and Technology, Shanghai, China.

Her research interests include millimeter-wave and THz spare imaging technology, especially THz synthetic-aperture radar imaging algorithm and matrix completion technique.

Ping Li received the Ph.D. degree from Northwestern Polytechnical University, Xi'an, China, in 2006.

She is currently a Researcher with the University of Shanghai for Science and Technology, Shanghai, China. Her research interests include millimeter-wave and terahertz-wave technology, especially with the terahertz imaging system.

Yiming Zhu received the bachelor's degree in applied physics and the Ph.D. degree in electronic engineering from Shanghai Jiao Tong University, Shanghai, China, in 2002 and 2008, respectively.

In 2003, he was an Assistant Researcher with the Research Center for Advanced Science and Technology, University of Tokyo, Tokyo, Japan. He is currently a Professor with the University of Shanghai for Science and Technology, Shanghai. His research interests include ultrafast optics, ultrafast electronics, and terahertz technology.